



A modified Stillinger–Weber potential-based hyperelastic constitutive model for nonlinear elasticity



Zhennan Zhang^{a,*}, Yaxiong Chen^a, Hong Zheng^b

^a School of Naval Architecture, Ocean and Civil Engineering, Shanghai Jiao Tong University, Shanghai 200240, China

^b Institute of Rock and Soil Mechanics, Chinese Academy of Sciences, Wuhan 430071, China

ARTICLE INFO

Article history:

Received 29 July 2013

Received in revised form 31 December 2013

Available online 10 January 2014

Keywords:

Stillinger–Weber potential

Constitutive model

Continuum

Fracture simulation

Quasi-brittle material

ABSTRACT

The Stillinger–Weber (SW) potential, which is a combination of the two- and three-body interaction, states that the bond energy is not only related to the distance between atoms, but also related to the bond angles subtended by this given bond and other bonds. The bond energy mechanism presented by the SW potential is different from that by the classical potentials, such as the Lennard–Jones, Tersoff and Embedded Atom potentials. Different micro energy mechanism reveals different micro fracture mechanism. The original SW potential takes the ‘ideal’ tetrahedral angle as the reference value of each bond angle in the current configuration, which makes it only applicable to the silicon materials. However, the micro fracture mechanism revealed by the SW potential should not be confined to the silicon materials. To extend the SW potential to a wider range of materials, the value of the bond angle in the reference configuration, not the ‘ideal’ tetrahedral angle, is taken as the reference value of this bond angle in the current configuration. Based on this modified SW potential, a constitutive model is developed. By this way, the micro fracture mechanism invoked by the SW potential is incorporated into the constitutive relation. Through this proposed constitutive model, it is found that the Hookean matrix derived from the SW potential matches that of a linear elastic continuum, which suggests that there exists a corresponding relationship between the micro physical parameters of SW potential and the macro material constants. The corresponding micro–macro parameter relationship is derived in this paper. To examine the application of this method to other materials, it is used to simulate the mixed fracture growth in concrete under static and dynamic load. The simulation results suggest that the present method can capture the characters of fracture growth in the quasi-brittle materials. It suggests that the constitutive model based on the modified SW potential can be applied to materials other than silicon. Because the interatomic potential-incorporated constitutive model makes the fracture criterion as the intrinsic property of a constitutive relation, it presents many advantages in fracture simulation. This paper enriches the constitutive relation with the micro fracture mechanism presented in SW potential, providing a new micro constitutive model for materials. Besides this, it also provides a feasible approach to calibrating the parameters of the SW potential for a certain material.

© 2014 Elsevier Ltd. All rights reserved.

1. Introduction

It is known that molecular dynamics is the most precise fracture simulation method by far. The underlying reason is that it can capture the micro fracture mechanism of material. But due to the length and time scale, it cannot be extended to the problems of engineering scale. A feasible approach to this problem is to develop a constitutive model based on the micro bond potential and build the micro fracture mechanism into the macro constitutive relation. By this way, the internal degrees of freedom can be dramatically reduced on the one hand. On the other hand, the main micro fracture mechanism contained in the micro bond potential can

be preserved in the constitutive relation. Thus, the interatomic potential-incorporated constitutive model has many advantages in fracture simulation. To develop the interatomic potential-incorporated constitutive model, the Cauchy–Born rule (Milstein, 1980; Tadmor et al., 1996) provides an important approach to bridging the gap between the degrees of freedom of ‘atoms’ and the macro displacement field. According to the Cauchy–Born rule, a micro bond in the reference configuration can be mapped to the current configuration by the deformation gradient. And then in the framework of hyperelastic theory, the constitutive relation based on the micro bond potential is derived. He and Li (2012) proposed a micro mechanical constitutive model based an Embedded Atom potential (Daw and Baskes, 1983). Li et al. (2012) and Zeng and Li (2010) embedded the Lennard–Jones potential into the constitutive relation of the bulk material and developed the multiscale cohesive

* Corresponding author. Tel./fax: +86 21 34204346.

E-mail address: zhennanzhang@sjtu.edu.cn (Z. Zhang).

zone based on the coarse grained depletion potential for the crystalline solids. The merit of Li and Zeng' work is that both the constitutive models of the bulk material and the cohesive zone are based on a certain interatomic potential. Before a critical yielding point, the cohesive zone has the same mechanical properties as the bulk material. After this yielding point, the cohesive zone softens whereas the bulk material does not, which automatically confines the fracture in the cohesive zone. The fracture mechanism represented by their models is more physically sound. To study the nanotube modulus, Zhang et al. (2002) incorporated the many-body potential (Tersoff, 1988; Brenner, 1990) into the continuum constitutive relation. Liu et al. (2010) embedded not only the interatomic potential, but also two energy-based lattice instability criteria into the constitutive relation to capture the stress-driven instabilities of a perfect crystal. These methods are all based on the rigorous realistic interatomic potentials. The macro mechanical properties of material can be directly obtained by the micro bond parameters, providing an approach to linking the micro and macro scale mechanical properties.

Different from the methods mentioned above, the virtual internal bond (VIB) (Gao and Klein, 1998) develops the constitutive relation of the bulk material based on a postulated microstructure, which consists of randomized material particles. These material particles are connected with virtual internal bonds. The micro cohesive bond network of VIB is an abstract of the real microstructure of material. To compute the strain energy density of a representative volume element, a bond distribution density function is introduced. The macro constitutive relation is derived by a homogenization process. The micro bond parameters are calibrated through the macro material constants. The particle in VIB is unnecessary to be the real atom and the potential is also unnecessary to be the realistic interatomic potential, which makes the VIB method more flexible. Though the VIB cannot represent the specific lattice structure in its constitutive relation due to the homogenization process, it can capture the cohesive properties between micro particles through a phenomenological two-parameter potential. Hence, it also presents many advantages in fracture simulation. Later, Zhang and Ge (2005, 2006) considered the bond rotation effect by introducing the shear bond into the VIB while Zhang and Gao (2012) directly used the Xu–Needleman potential (Xu and Needleman, 1994) to simultaneously account for the effect of bond stretch and bond rotation. Due to accounting for the bond rotation effect, the VIB can be applied to materials with variable Poisson ratios. Along this line, there are many other micro–macro constitutive models (e.g. Chang and Hicher, 2005; Misra and Yang, 2010; Zhao and Zhao, 2012).

The advantages of the interatomic potential-incorporated constitutive model in fracture simulation stem from the fact that the fracture criterion invoked by the interatomic potential has been embedded into the constitutive relation as an intrinsic property. Different micro bond potential presents different micro energy mechanism, therefore, reveals different micro fracture mechanism. For example, the Lennard–Jones potential holds that the bond energy is only related to the distance between atoms. The Tersoff potential insists that the bond energy is not only related to the distance between two atoms, but also related to the other atoms. It accounts for the effect of other atoms via the coefficients of the two-body potential. The Embedded Atom potential states that the interaction between atoms is not only determined by the distance between atoms, but also related to the electron charge density of other atoms. Hence, it can be written into the combination of the two-body potential and the embedding function. The micro fracture mechanisms invoked in these classical interatomic potentials have been incorporated into the constitutive models mentioned above. But these micro fracture mechanisms are still inadequate to predict the fracture behaviors of a wider range of materials. Thus, more micro fracture mechanisms are required.

The Stillinger–Weber (SW) potential (Stillinger and Weber, 1985) presents a different micro energy mechanism than those interatomic potentials mentioned above. It holds that the bond energy between two atoms is not only related to their distance, but also related to all the bond angles subtended by the given bond and other bonds. It is a combination of the two- and three-body interaction. Such micro energy mechanism has never been incorporated into the constitutive relation so far. It is undoubted that the SW potential has been successfully applied to the crystalline silicon materials since it was born. One of the underlying reasons lies in that the three-body interaction of SW potential takes the 'ideal' tetrahedral angle as the reference value of each bond angle in the current configuration. However, the micro energy mechanism presented in SW potential should not be confined to the silicon materials. To extend the SW potential to other materials and enrich the constitutive relation with diverse micro fracture mechanisms, we make a modification on the SW potential in this paper. That is the value of the bond angle in the reference configuration, not the 'ideal' tetrahedral angle, is taken as the reference value of this bond angle in the current configuration. Based on this modified SW potential, we develop a constitutive model. It is found that the proposed constitutive relation can be used to the materials other than the silicon and there exists a corresponding relationship between the micro physical parameters of SW potential and the macro material constants.

2. Brief review on the original SW potential and its modified version

In molecular dynamics, the potential energy function of a discrete system with N particles can be written into

$$\Phi(1, \dots, N) = \sum_i \Phi_1(i) + \sum_{i < j} \Phi_2(i, j) + \sum_{\substack{i, j, k \\ i < j < k}} \Phi_3(i, j, k) + \dots + \Phi_N(i, \dots, N) \quad (1)$$

in which the term Φ_1 means the single-particle potential, describing wall and external forces to which the system is subject; Φ_2 the pair (two-body) potential; Φ_3 the three-body potential accounting for the bond angle effect; Φ_N the N -body potential. In order to make Eq. (1) useful in the usual types of theoretical modeling, it is necessary that the component functions Φ_n converge quickly to zero with increasing n (Stillinger and Weber, 1985).

The pairwise potential Φ_2 is the simplest one which is the function of the distance between the two related particles. It only accounts for the bond stretch effect. If such potential is reduced to the linear case, only one parameter, say the bond 'stiffness' coefficient, governs the entire discrete system. However, on the macro scale, two parameters (Young's modulus and the Poisson ratio) characterize a linear elastic medium. The number of micro parameters does not match that of the macro parameters. Hence, the discrete system described by the pairwise potential has a fixed Poisson ratio.

In the SW potential (Stillinger and Weber, 1985; Pizzagalli et al., 2013), the total energy Φ is obtained as a combination of two- and three-body interactions

$$\Phi = \sum_{i < j} \Phi_2(r_{ij}) + \sum_{\substack{i, j, k \\ i < j < k}} \Phi_3(r_{ij}, r_{ik}, \theta_{ijk}) \quad (2)$$

The two- and three-body interaction of SW potential are respectively

$$\begin{aligned} \Phi_2(r_{ij}) &= A \left[B \left(\frac{\ell_0}{r_{ij}} \right)^p - \left(\frac{\ell_0}{r_{ij}} \right)^q \right] \exp \left(\frac{1}{r_{ij}/\ell_0 - r_0^*} \right) \\ \Phi_3(r_{ij}, r_{ik}, \theta_{ijk}) &= \lambda \left(\cos \theta_{ijk} + \frac{1}{3} \right)^2 \exp \left(\frac{\gamma}{r_{ij}/\ell_0 - r_0^*} \right) \exp \left(\frac{\gamma}{r_{ik}/\ell_0 - r_0^*} \right) \end{aligned} \quad (3)$$

in which θ_{ijk} is the bond angle subtended by the bond \mathbf{r}_{ij} , \mathbf{r}_{ik} at vertex i ; r_{ij} the bond length of bond \mathbf{r}_{ij} ; r_0^* the cutoff radii; the $1/3$ being the minus cosine of the ‘ideal’ tetrahedral angle. The parameters A, λ , here, implicitly contain the energy scaling parameter ε of the original two- and three-body interaction of Stillinger and Weber (1985).

Eq. (2) indicates that the bond energy due to bond rotation is related to all the bond angles subtended by this given bond and other bonds. For example, in a discrete system with N particles shown in Fig. 1, let \mathbf{r}_i denote the bond vector \mathbf{r}_{ij} and r_i its length; \mathbf{r}_j the bond vector \mathbf{r}_{ik} and r_j its length; θ_{ij} the bond angle θ_{ijk} . The energy of the bond \mathbf{r}_i due to bond rotation is related to all its conjugate bonds $\mathbf{r}_j^1, \mathbf{r}_j^2, \dots, \mathbf{r}_j^{N-2}$, whose total number is $N-2$. So, Eq. (2) can be rewritten as

$$\Phi = \frac{1}{2} \cdot \sum_{i=1}^{N(N-1)} \Phi_2(r_i) + \frac{1}{2} \cdot \sum_{i=1}^{N(N-1)} \sum_{j \neq i}^{N-2} \Phi_3(r_i, r_j, \theta_{ij}) \quad (4)$$

It is obvious that the micro energy mechanism presented in the SW potential is different from the other potentials, as analyzed in the Introduction Section. According to Eq. (3), the three-body interaction of the original SW potential takes the ‘ideal’ tetrahedral angle as the reference value of each bond angle in the current configuration. That means the ideal tetrahedral lattice structure is the most stable one. This makes SW potential suitable for the silicon materials. However, the micro energy mechanism should not be confined to the silicon materials. To extend the SW potential to other materials, we should wipe off the topology information of SW potential in that the value of the bond angle in the reference configuration, not the ‘ideal’ tetrahedral angle, should be taken as the reference value of this bond angle in the current configuration.

Additionally, in the up-scaling constitutive modeling method by homogenization, the material particles are usually assumed to be randomly distributed in a representative element and the reference configuration should be an equilibrium system. However, the reference configuration of the randomized particles governed by the original SW potential is not an equilibrium system and would be forced into a structured configuration, shown in Fig. 2. Hence, we should, at first, modify the SW potential.

According to the analysis above, the two- and three-body interaction in the modified SW potential should read

$$\begin{aligned} \Phi_2(r_i/\ell_0) &= \Phi_2(\tilde{r}_i) = A(B\tilde{r}_i^{-p} - \tilde{r}_i^{-q}) \exp(h_i^{-1}) \\ \Phi_3(r_i/\ell_0, r_j/\ell_0, \theta_{ij}) &= \Phi_3(\tilde{r}_i, \tilde{r}_j, \theta_{ij}) = \lambda(\cos \theta_{ij} - \cos \theta_{j0})^2 \exp(\gamma h_i^{-1} + \gamma h_j^{-1}) \end{aligned} \quad (5)$$

in which \tilde{r}_i, \tilde{r}_j are the normalized bond length, $\tilde{r}_i = r_{ij}/\ell_0$, $\tilde{r}_j = r_{ik}/\ell_0$; $h_i = \tilde{r}_i - r_0^*$, $h_j = \tilde{r}_j - r_0^*$; θ_{j0} means the bond angle subtended by bond \mathbf{r}_i and \mathbf{r}_j in the reference configuration. The derivatives of Φ_2, Φ_3 with respect to \tilde{r} and θ_{ij} are listed in Appendix A.

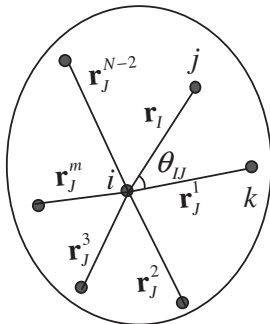


Fig. 1. The conjugate bond vectors subtended at a given particle i in a discrete system with N particles. (The total particle number is N . The bond number of \mathbf{r}_i is $N(N-1)$ and its conjugate bond number is $N-2$ with the condition $\mathbf{r}_{ij} \neq \mathbf{r}_{ji}$.)

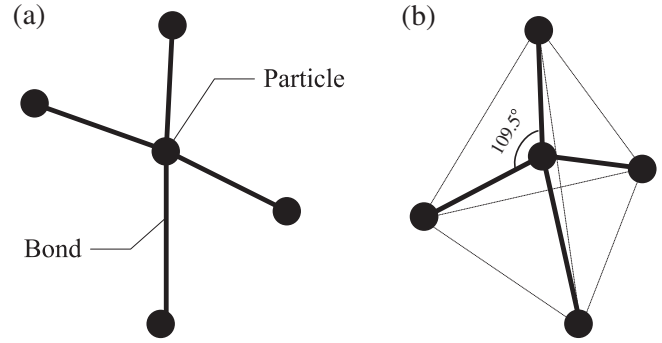


Fig. 2. The particle configuration (a) the randomized configuration in which the particles are randomly scattered; (b) the structured configuration in which the bonds form an ideal tetrahedron. The configuration transformation from (a) to (b) is driven by the three-body interaction Φ_3 .

3. General formula of constitutive relation

To develop a constitutive model, let's take a representative volume element as the analysis object. On the micro scale, the representative volume element of a continuum is considered to consist of randomized material particles, shown in Fig. 3. In the representative volume element, $\mathbf{r}_i, \mathbf{r}_j$ are two conjugated vectors subtended at a certain vertex in the current configuration, whose orientation vectors in the reference configuration are $\xi = (\sin \alpha \cos \varphi, \sin \alpha \sin \varphi, \cos \alpha)^T$ and $\eta = (\sin \bar{\alpha} \cos \bar{\varphi}, \sin \bar{\alpha} \sin \bar{\varphi}, \cos \bar{\alpha})^T$ in the spherical coordinates, respectively. Assume that all the bonds in the reference configuration have the same length ℓ_0 , shown in Fig. 3a. According to Cauchy–Born rule, the lengths of the bond $\mathbf{r}_i, \mathbf{r}_j$ are respectively calculated as

$$\begin{aligned} r_i &= \ell_0 \sqrt{\xi^T \mathbf{F}^T \mathbf{F} \xi} = \ell_0 \sqrt{\xi^T (2\mathbf{E} + \mathbf{I}) \xi} \\ r_j &= \ell_0 \sqrt{\eta^T \mathbf{F}^T \mathbf{F} \eta} = \ell_0 \sqrt{\eta^T (2\mathbf{E} + \mathbf{I}) \eta} \end{aligned} \quad (6)$$

in which \mathbf{F} is the deformation gradient; \mathbf{E} the Lagrangian strain tensor and \mathbf{I} the identity tensor.

And the bond angle θ_{ij} is calculated as

$$\begin{aligned} \theta_{ij} &= \arccos \left(\frac{\xi^T \mathbf{F}^T \mathbf{F} \eta}{\sqrt{\xi^T \mathbf{F}^T \mathbf{F} \xi} \cdot \sqrt{\eta^T \mathbf{F}^T \mathbf{F} \eta}} \right) \\ &= \arccos \left(\frac{\xi^T (2\mathbf{E} + \mathbf{I}) \eta}{\sqrt{\xi^T (2\mathbf{E} + \mathbf{I}) \xi} \cdot \sqrt{\eta^T (2\mathbf{E} + \mathbf{I}) \eta}} \right) \end{aligned} \quad (7)$$

According to Eq. (4), the strain energy density of the representative volume element is

$$W = \frac{1}{V} \cdot \frac{1}{2} \cdot \sum_{i=1}^{N(N-1)} \Phi_2(r_i) + \frac{1}{V} \cdot \frac{1}{2} \cdot \sum_{i=1}^{N(N-1)} \sum_{j \neq i}^{N-2} \Phi_3(r_i, r_j, \theta_{ij}) \quad (8)$$

where V is the volume of the representative volume element and N is the total particle number in a representative volume element.

If the bonds are uniformly distributed and the number is large enough, the strain energy density (Eq. (8)) can be written into the integral form

$$W = \frac{1}{2V} \cdot \langle \Phi_2(r_i) \cdot D_i \rangle_2 + \frac{1}{2V} \cdot \langle \Phi_3(r_i, r_j, \theta_{ij}) \cdot D_i \cdot D_j \rangle_3 \quad (9)$$

in which the operators $\langle \dots \rangle_2, \langle \dots \rangle_3$ are

$$\begin{aligned} \langle \dots \rangle_2 &= \begin{cases} \int_0^{2\pi} \int_0^\pi (\dots) \cdot \sin \alpha \cdot d\alpha d\varphi & \text{for 3D-cases} \\ \int_0^{2\pi} (\dots) \cdot d\alpha & \text{for 2D-cases} \end{cases} \\ \langle \dots \rangle_3 &= \begin{cases} \int_0^{2\pi} \int_0^\pi \int_0^\pi \int_0^\pi (\dots) \cdot \sin \bar{\alpha} \cdot \sin \alpha \cdot d\bar{\alpha} d\varphi d\alpha d\varphi & \text{for 3D-cases} \\ \int_0^{2\pi} \int_0^\pi (\dots) \cdot d\bar{\alpha} d\alpha & \text{for 2D-cases} \end{cases} \end{aligned} \quad (10)$$

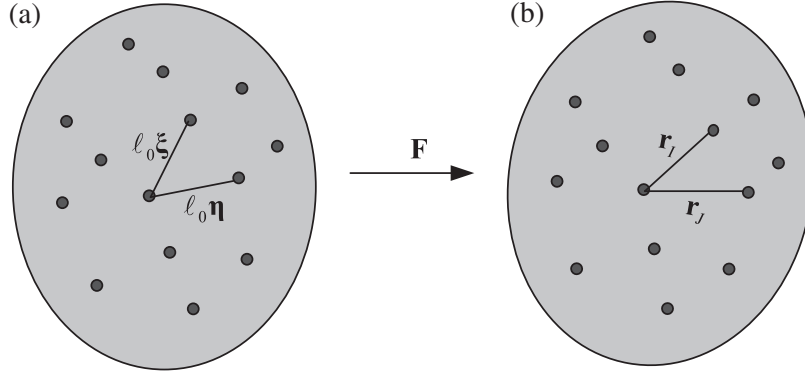


Fig. 3. The representative volume element in (a) the reference configuration and (b) the current configuration.

and D_i , D_j are the distribution densities of bond \mathbf{r}_i and bond \mathbf{r}_j , respectively,

$$D_i = \begin{cases} \frac{N(N-1)}{4\pi} & \text{for 3D-cases} \\ \frac{N(N-1)}{2\pi} & \text{for 2D-cases} \end{cases}, \quad D_j = \begin{cases} \frac{N-2}{4\pi} & \text{for 3D-cases} \\ \frac{N-2}{2\pi} & \text{for 2D-cases} \end{cases} \quad (11)$$

For the detailed derivation from Eq. (8) to Eq. (9), refer to Appendix B.

Within the framework of hyperelastic theory, by Eq. (9), the stress tensor is derived as

$$S_{ij} = \frac{\partial W}{\partial E_{ij}} = \frac{D_i}{2V} \cdot \left\langle \frac{\partial \Phi_2}{\partial r_i} \cdot \frac{\partial r_i}{\partial E_{ij}} \right\rangle_2 + \frac{D_i D_j}{2V} \cdot \left\langle \frac{\partial \Phi_3}{\partial r_i} \cdot \frac{\partial r_i}{\partial E_{ij}} + \frac{\partial \Phi_3}{\partial r_j} \cdot \frac{\partial r_j}{\partial E_{ij}} + \frac{\partial \Phi_3}{\partial \theta_{ij}} \cdot \frac{\partial \theta_{ij}}{\partial E_{ij}} \right\rangle_3 \quad (12)$$

and the tangent modulus is derived as

$$\Gamma_{ijkl} = \frac{\partial^2 W}{\partial E_{ij} \partial E_{kl}} = \frac{D_i}{2V} \cdot \left\langle \frac{\partial^2 \Phi_2}{\partial r_i^2} \cdot \frac{\partial r_i}{\partial E_{ij}} \cdot \frac{\partial r_i}{\partial E_{kl}} + \frac{\partial \Phi_2}{\partial r_i} \cdot \frac{\partial^2 r_i}{\partial E_{ij} \partial E_{kl}} \right\rangle_2 + \frac{D_i D_j}{2V} \cdot \left\langle \frac{\partial^2 \Phi_3}{\partial r_i^2} \cdot \frac{\partial r_i}{\partial E_{ij}} \cdot \frac{\partial r_i}{\partial E_{kl}} + \frac{\partial \Phi_3}{\partial r_i} \cdot \frac{\partial^2 r_i}{\partial E_{ij} \partial E_{kl}} + \frac{\partial^2 \Phi_3}{\partial r_j^2} \cdot \frac{\partial r_j}{\partial E_{ij}} \cdot \frac{\partial r_j}{\partial E_{kl}} + \frac{\partial \Phi_3}{\partial r_j} \cdot \frac{\partial^2 r_j}{\partial E_{ij} \partial E_{kl}} + \frac{\partial^2 \Phi_3}{\partial \theta_{ij}^2} \cdot \frac{\partial \theta_{ij}}{\partial E_{ij}} \cdot \frac{\partial \theta_{ij}}{\partial E_{kl}} + \frac{\partial \Phi_3}{\partial \theta_{ij}} \cdot \frac{\partial^2 \theta_{ij}}{\partial E_{ij} \partial E_{kl}} \right\rangle_3 \quad (13)$$

Eqs. (12) and (13) are the constitutive relation in the finite deformation cases. In the small deformation cases, the Lagrangian strain is reduced to the Cauchy strain, i.e. $\mathbf{E} \rightarrow \boldsymbol{\varepsilon}$, and accordingly $\mathbf{S} \rightarrow \boldsymbol{\sigma}$. Then the deformed bond length can be calculated as

$$r_i = \ell_0 \varepsilon_{mn} \xi_m \xi_n + \ell_0 \quad (14)$$

$$r_j = \ell_0 \varepsilon_{mn} \eta_m \eta_n + \ell_0$$

According to Eq. (7), the bond angle is highly nonlinear with the strain tensor. Its derivative with respect to strain would be extremely complicated. In the small deformation cases, it can be simplified by expanding bond angle into Taylor series and taking the first-order term as its approximate value. That is

$$\theta_{ij}(\varepsilon_{ij}) \approx \theta_{ij}(0) + \Theta_{ij} \varepsilon_{ij} \Rightarrow \theta_{ij} - \theta_{ij0} \approx \Theta_{ij} \varepsilon_{ij} \quad (15)$$

in which

$$\Theta_{ij} = \theta'_{ij}(\mathbf{0}) = -\frac{1}{\sqrt{1 - (\xi^T \boldsymbol{\eta})^2}} \cdot (2\xi_i \eta_j - \xi^T \boldsymbol{\eta} \cdot \xi_i \xi_j - \xi^T \boldsymbol{\eta} \cdot \eta_i \eta_j) \quad (16)$$

For the detailed derivation of Eqs. (15) and (16), see Appendix C.

Substituting Eqs. (14)–(16) into Eqs. (12) and (13), the stress tensor and the tangent modulus tensor in the small deformation cases can be respectively derived

$$\sigma_{ij} = \frac{D_i}{2V} \cdot \left\langle \frac{\partial \Phi_2}{\partial r_i} \cdot \ell_0 \xi_i \xi_j \right\rangle_2 + \frac{D_i D_j}{2V} \cdot \left\langle \frac{\partial \Phi_3}{\partial r_i} \cdot \ell_0 \xi_i \xi_j + \frac{\partial \Phi_3}{\partial r_j} \cdot \ell_0 \eta_i \eta_j + \frac{\partial \Phi_3}{\partial \theta_{ij}} \cdot \Theta_{ij} \right\rangle_3 \quad (17)$$

and

$$K_{ijkl} = \frac{D_i}{2V} \cdot \left\langle \frac{\partial^2 \Phi_2}{\partial r_i^2} \cdot \ell_0^2 \xi_i \xi_j \xi_k \xi_l \right\rangle_2 + \frac{D_i D_j}{2V} \cdot \left\langle \frac{\partial^2 \Phi_3}{\partial r_i^2} \cdot \ell_0^2 \xi_i \xi_j \xi_k \xi_l + \frac{\partial^2 \Phi_3}{\partial r_j^2} \cdot \ell_0^2 \eta_i \eta_j \eta_k \eta_l + \frac{\partial^2 \Phi_3}{\partial \theta_{ij}^2} \cdot \Theta_{ij} \Theta_{kl} \right\rangle_3 \quad (18)$$

4. Specific constitutive relation with determined micro parameters

4.1. Parameter calibration

Substituting Eq. (5) into Eqs. (17) and (18), the constitutive relation can be obtained. But in Eq. (5) there are totally 8 parameters, i.e. $\{A, \lambda, B, p, q, \gamma, r_0^*, \ell_0\}$. The key point is that what values these parameters should take so that the constitutive relation can represent an equivalent continuum.

To calibrate the micro parameters of Eq. (5), we firstly substitute Eq. (5) into the tangent modulus function (Eq. (18)) and then consider it under the undeformed state. By making the Hookean matrix of Eq. (18) equal that of the linear elastic solid, the micro parameters of bond potential can be calibrated.

In the undeformed state ($r_i = r_j = \ell_0$, $\theta_{ij} = \theta_{ij0}$), by Eq. (5), the following relationship holds

$$\frac{\partial \Phi_2}{\partial r_i} \Big|_{r_i=\ell_0} = 0 \Rightarrow B = \frac{h_0^{-2} + q}{h_0^{-2} + p} \quad (19)$$

with $h_0 = 1 - r_0^*$.

The second derivatives of Φ_2 , Φ_3 with respect to r and θ_{ij} are

$$\begin{aligned} \frac{\partial^2 \Phi_2}{\partial r_i^2} \Big|_{r_i=\ell_0} &= A \cdot \exp(h_0^{-1}) \cdot [B(p^2 + p + ph_0^{-2} + 2h_0^{-3}) - (q^2 + q + qh_0^{-2} + 2h_0^{-3})] \ell_0^{-2} \\ \frac{\partial^2 \Phi_3}{\partial r_i^2} \Big|_{r_i=\ell_0} &= 0, \quad \frac{\partial^2 \Phi_3}{\partial r_j^2} \Big|_{r_j=\ell_0} = 0 \\ \frac{\partial^2 \Phi_3}{\partial \theta_{ij}^2} \Big|_{\theta_{ij}=\theta_{ij0}} &= \lambda \exp(2\gamma h_0^{-1}) \cdot 2 \sin^2 \theta_{ij0} \end{aligned} \quad (20)$$

Substituting Eq. (20) into Eq. (18), we can obtain

$$K_{ijkl} \Big|_{\boldsymbol{\varepsilon}=\mathbf{0}} = \bar{K}_n \cdot \langle \xi_i \xi_j \xi_k \xi_l \rangle_2 + \bar{K}_s \cdot \langle \sin^2 \theta_{ij0} \cdot \Theta_{ij} \Theta_{kl} \rangle_3 \quad (21)$$

in which

$$\begin{aligned}\bar{k}_n &= \frac{D_1 A}{2V} \cdot \exp(h_0^{-1}) \cdot [B(p^2 + p + ph_0^{-2} + 2h_0^{-3}) - (q^2 + q + qh_0^{-2} + 2h_0^{-3})] \\ \bar{k}_s &= \frac{D_1 D_2 \lambda}{2V} \cdot 2 \exp(2\gamma h_0^{-1})\end{aligned}\quad (22)$$

The Hookean matrix of Eq. (21) can be written as

$$\Omega^s = \bar{k}_n \cdot \Omega_L^s + \bar{k}_s \cdot \Omega_R^s \quad (23)$$

in which the Hookean matrix Ω^s is defined as $[\sigma_{11}, \sigma_{22}, \sigma_{33}, \sigma_{12}, \sigma_{23}, \sigma_{31}]^T = \Omega^s [\varepsilon_{11}, \varepsilon_{22}, \varepsilon_{33}, 2\varepsilon_{12}, 2\varepsilon_{23}, 2\varepsilon_{31}]^T$; the sub-Hookean matrixes Ω_L^s and Ω_R^s are respectively obtained by calculating the integral $\langle \xi_i \xi_j \xi_k \xi_l \rangle_2$ and $\langle \sin^2 \theta_{ij0} \cdot \Theta_{ij} \Theta_{kl} \rangle_3$.

If the micro mechanics model can represent an equivalent continuum, the following relationship should hold.

$$\Omega^s = \Omega^c \quad (24)$$

where Ω^c is the Hookean matrix of the equivalent continuum.

4.1.1. 3D case

In 3D cases, by integrating $\langle \xi_i \xi_j \xi_k \xi_l \rangle_2$ and $\langle \sin^2 \theta_{ij0} \cdot \Theta_{ij} \Theta_{kl} \rangle_3$, the sub-Hookean matrixes Ω_L^s and Ω_R^s can be obtained as

$$\Omega_L^s = \frac{4\pi}{15} \begin{bmatrix} 3 & 1 & 1 & 0 & 0 & 0 \\ 1 & 3 & 1 & 0 & 0 & 0 \\ 1 & 1 & 3 & 0 & 0 & 0 \\ 0 & 0 & 0 & 1 & 0 & 0 \\ 0 & 0 & 0 & 0 & 1 & 0 \\ 0 & 0 & 0 & 0 & 0 & 1 \end{bmatrix}, \quad \Omega_R^s = \frac{128\pi^2}{225} \begin{bmatrix} 4 & -2 & -2 & 0 & 0 & 0 \\ -2 & 4 & -2 & 0 & 0 & 0 \\ -2 & -2 & 4 & 0 & 0 & 0 \\ 0 & 0 & 0 & 3 & 0 & 0 \\ 0 & 0 & 0 & 0 & 3 & 0 \\ 0 & 0 & 0 & 0 & 0 & 3 \end{bmatrix} \quad (25)$$

The nonzero components of the symmetrical Hookean matrix Ω^c of a linear elastic continuum are

$$\begin{aligned}\Omega_{11}^c &= \Omega_{22}^c = \Omega_{33}^c = \frac{E(1-\nu)}{(1+\nu)(1-2\nu)} \\ \Omega_{12}^c &= \Omega_{13}^c = \Omega_{23}^c = \frac{E\nu}{(1+\nu)(1-2\nu)} \\ \Omega_{44}^c &= \Omega_{55}^c = \Omega_{66}^c = \frac{E}{2(1+\nu)}\end{aligned}\quad (26)$$

in which E is the Young's modulus and ν is the Poisson ratio.

By Eqs. (22)–(24) and (26), we have

$$\begin{aligned}\frac{12\pi}{15} \cdot \bar{k}_n + \frac{512\pi^2}{225} \cdot \bar{k}_s &= \frac{E(1-\nu)}{(1+\nu)(1-2\nu)} \\ \frac{4\pi}{15} \cdot \bar{k}_n - \frac{256\pi^2}{225} \cdot \bar{k}_s &= \frac{E\nu}{(1+\nu)(1-2\nu)} \\ \frac{4\pi}{15} \cdot \bar{k}_n + \frac{384\pi^2}{225} \cdot \bar{k}_s &= \frac{E}{2(1+\nu)}\end{aligned}\quad (27)$$

By Eq. (27), the hybrid bond parameters are derived as

$$\bar{k}_n = \frac{3E}{4\pi(1-2\nu)}, \quad \bar{k}_s = \frac{45E(1-4\nu)}{256\pi^2(1+\nu)(1-2\nu)} \quad (28)$$

4.1.2. 2D case

In 2D cases, the matrixes Ω_L^m and Ω_R^m are respectively

$$\Omega_L^m = \frac{\pi}{4} \begin{bmatrix} 3 & 1 & 0 \\ 1 & 3 & 0 \\ 0 & 0 & 1 \end{bmatrix}, \quad \Omega_R^m = \frac{3\pi^2}{4} \begin{bmatrix} 1 & -1 & 0 \\ -1 & 1 & 0 \\ 0 & 0 & 1 \end{bmatrix} \quad (29)$$

The Hookean matrix Ω^c of a linear elastic continuum in 2D cases is

$$\Omega^c = \frac{E_0}{1-\nu_0^2} \begin{bmatrix} 1 & \nu_0 & 0 \\ \nu_0 & 1 & 0 \\ 0 & 0 & (1-\nu_0)/2 \end{bmatrix} \quad (30)$$

in which $E_0 = E, \nu_0 = \nu$ for plane-stress problems and $E_0 = E/(1-\nu^2), \nu_0 = \nu/(1-\nu)$ for plane-strain problems.

By Eqs. (22)–(24), (29) and (30), the micro bond parameters are derived as

$$\bar{k}_n = \frac{E_0}{\pi(1-\nu_0)}, \quad \bar{k}_s = \frac{E_0(1-3\nu_0)}{3\pi^2(1-\nu_0^2)} \quad (31)$$

By Eqs. (22), (28), (31), the potential parameters are calibrated as

$$\begin{aligned}A &= \frac{2V}{D_1} \cdot \frac{\bar{k}_n}{c \exp(h_0^{-1})}, \quad \lambda = \frac{V}{D_1 D_2} \cdot \frac{\bar{k}_s}{\exp(2\gamma h_0^{-1})} \\ c &= B(p^2 + p + ph_0^{-2} + 2h_0^{-3}) - (q^2 + q + qh_0^{-2} + 2h_0^{-3})\end{aligned}\quad (32)$$

4.2. Comparative analysis with VMIB and AVIB

Comparing Eqs. (28) and (31) with the stiffness coefficients in the previous works of the virtual multidimensional internal bond (VMIB) (Zhang and Ge, 2006) and the augmented virtual internal bond (AVIB) (Zhang and Gao, 2012), it is found that they have the same form. This is because they have the same physical meanings, namely that \bar{k}_n stands for the coefficient of stiffness due to the bond stretch whereas the \bar{k}_s the coefficient of stiffness due to the bond rotation. Here, the bond rotation has excluded the rigid body rotation. The three methods (the VMIB, the AVIB, the present study) account for the bond rotation effect in the constitutive relation, but the measures they take are different.

In the VMIB, the bond rotation is characterized by three angles that the bond rotates towards the three coordinate axes respectively. The three angles in Zhang and Ge (2006) are respectively calculated as $\beta_1 = \xi_i \varepsilon_{ij} \eta_j', \beta_2 = \xi_i \varepsilon_{ij} \eta_j'', \beta_3 = \xi_i \varepsilon_{ij} \eta_j'''$ in which ε is the strain tensor of the representative volume element; η', η'', η''' are three vectors perpendicular to the bond vector ξ , $\eta' = \xi \times (\bar{\mathbf{x}}_1 \times \xi)$,

$\eta'' = \xi \times (\bar{\mathbf{x}}_2 \times \xi)$, $\eta''' = \xi \times (\bar{\mathbf{x}}_3 \times \xi)$ with $\bar{\mathbf{x}}_i$ being the unit orientation vector of x_i - axes. The energy due to the bond rotation is identified as $W_s = k_s(\beta_1^2 + \beta_2^2 + \beta_3^2)/2$. In VMIB, the energies due to the bond stretch and the bond rotation are independent. The total energy of a given bond is calculated as $W = W_n + W_s = k_n(\xi^T \varepsilon \xi)/2 + k_s(\beta_1^2 + \beta_2^2 + \beta_3^2)/2$, in which $k_n(\xi^T \varepsilon \xi)/2$ means the energy due to bond stretch. Here, we have to point out that the vectors η', η'', η''' in Zhang and Ge (2006) are not the unit one. They should be normalized as $\eta' = \eta'/\|\eta'\|, \eta'' = \eta''/\|\eta''\|, \eta''' = \eta'''/\|\eta'''\|$ where $\|\cdot\|$ denotes the norm of a vector.

In the AVIB, the rotation angle of a given bond ξ is directly calculated as $\beta = \sqrt{\xi^T \varepsilon^T \xi \xi - (\xi^T \varepsilon \xi)^2}$ and the bond stretch is calculated as $\Delta_n = \xi^T \varepsilon \xi \ell_0$ with ℓ_0 being the undeformed bond length. Through the Xu–Needleman potential (Xu and Needleman, 1994), the energy of this given bond is identified as $W(\Delta_n, \beta) = \phi_n - \phi_n \exp(-\Delta_n/\delta_n)(1 + \Delta_n/\delta_n)[1 - q + q \exp(-\beta^2 \ell_0^2/\delta_r^2)]$ where $\phi_n, q, \delta_n, \delta_r$ are the micro parameters. In the AVIB, the energies due to the bond stretch and the bond rotation are no longer independent, but coupled together.

It is noted that in both the VMIB and the AVIB, the rotation effect of a given bond is independently accounted. However, in the present study, the bond rotation is accounted in a coupled manner. The bond rotation effect in the present study is related to all the bond angles subtended by this given bond and other bonds, which makes the bonds in a representative volume element coupled together. According to Eq. (4), the energy of a given bond \mathbf{r}_i due to bond rotation is identified as $W_s^i = \sum_{j \neq i}^{N-2} \Phi_3(r_i, r_j, \theta_{ij})$. Through the SW potential, the energy of the representative volume element is calculated as Eq. (4).

From the above analysis, it is obvious that the present study, the VMIB and the AVIB take different ways to characterize the bond rotation. Besides the characterization of bond rotation, the bond

energy potentials they employed are also different, namely that the VMIB takes the linear elastic potential, the AVIB takes the Xu–Needleman potential and the present study takes the SW potential. Different potential reveals different micro fracture mechanism. Thus, strictly speaking, the AVIB and the present study are not the nonlinear cases of VMIB since the bond rotation characterizations are different in the three methods. They take different ways to account for the bond rotation effect and incorporate different micro fracture mechanisms into their constitutive relation.

4.3. Constitutive relation with determined parameters

Substituting Eqs. (5) and (32) into Eqs. (17) and (18) respectively, we have the stress tensor

$$\sigma_{ij} = \frac{1}{c} \cdot \bar{k}_n \langle f_1 \cdot \xi_i \xi_j \rangle_2 + \frac{1}{2} \cdot \bar{k}_s \langle f_2 \cdot \xi_i \xi_j + f_3 \cdot \eta_i \eta_j + f_4 \cdot \Theta_{ij} \rangle_3 \quad (33)$$

in which

$$\begin{aligned} f_1 &= \exp(h_i^{-1} - h_0^{-1}) \left[(-Bp\tilde{r}_i^{-p-1} + q\tilde{r}_i^{-q-1}) - h_i^{-2} (B\tilde{r}_i^{-p} - \tilde{r}_i^{-q}) \right] \\ f_2 &= \exp(\gamma h_i^{-1} + \gamma h_j^{-1} - 2\gamma h_0^{-1}) (\cos \theta_{ij} - \cos \theta_{j0})^2 (-\gamma h_i^{-2}) \\ f_3 &= \exp(\gamma h_i^{-1} + \gamma h_j^{-1} - 2\gamma h_0^{-1}) (\cos \theta_{ij} - \cos \theta_{j0})^2 (-\gamma h_j^{-2}) \\ f_4 &= \exp(\gamma h_i^{-1} + \gamma h_j^{-1} - 2\gamma h_0^{-1}) \cdot 2(\cos \theta_{ij} - \cos \theta_{j0}) (-\sin \theta_{ij}) \\ \tilde{r}_i &= \xi^T \mathbf{E} \xi + 1, \quad \tilde{r}_j = \eta^T \mathbf{E} \eta + 1 \\ h_i &= \xi^T \mathbf{E} \xi + 1 - r_0^*, \quad h_j = \eta^T \mathbf{E} \eta + 1 - r_0^*, \quad h_0 = 1 - r_0^* \end{aligned} \quad (34)$$

and the tangent modulus

$$K_{ijkl} = \frac{1}{c} \cdot \bar{k}_n \langle g_1 \cdot \xi_i \xi_j \xi_k \xi_l \rangle_2 + \frac{1}{2} \cdot \bar{k}_s \langle g_2 \cdot \xi_i \xi_j \xi_k \xi_l + g_3 \cdot \eta_i \eta_j \eta_k \eta_l + g_4 \cdot \Theta_{ij} \Theta_{kl} \rangle_3 \quad (35)$$

in which

$$\begin{aligned} g_1 &= \exp(h_i^{-1} - h_0^{-1}) \left[Bp(p+1)\tilde{r}_i^{-p-2} - q(q+1)\tilde{r}_i^{-q-2} \right. \\ &\quad \left. + 2h_i^{-2} (Bp\tilde{r}_i^{-p-1} - q\tilde{r}_i^{-q-1}) + (h_i^{-4} + 2h_i^{-3}) (B\tilde{r}_i^{-p} - \tilde{r}_i^{-q}) \right] \\ g_2 &= \exp(\gamma h_i^{-1} + \gamma h_j^{-1} - 2\gamma h_0^{-1}) (\cos \theta_{ij} - \cos \theta_{j0})^2 (\gamma^2 h_i^{-4} + 2\gamma h_i^{-3}) \\ g_3 &= \exp(\gamma h_i^{-1} + \gamma h_j^{-1} - 2\gamma h_0^{-1}) (\cos \theta_{ij} - \cos \theta_{j0})^2 (\gamma^2 h_j^{-4} + 2\gamma h_j^{-3}) \\ g_4 &= \exp(\gamma h_i^{-1} + \gamma h_j^{-1} - 2\gamma h_0^{-1}) \cdot 2(1 - 2\cos^2 \theta_{ij} + \cos \theta_{j0} \cos \theta_{ij}) \end{aligned} \quad (36)$$

From Eqs. (33) and (35), we can find that such parameters as the volume of representative element, bond length, particle number, have been automatically eliminated from the final constitutive relation.

4.4. Influence of micro parameters on macro stress–strain response

For a given material, Young's modulus and Poisson ratio are determined. So in the constitutive relation (Eqs. (33) and (35)), there are four independent parameters in all, i.e. $\{p, q, \gamma, r_0^*\}$. The four parameters govern the shape of the stress–strain curve. So, we call them the shape parameters. We take $E = 10.0$ GPa, $\nu = 0.2$ as example. Referring to Lennard–Jones potential, we take $p = 12$, $q = 6$. When taking the shape parameters $p = 12$, $q = 6$, $r_0^* = 1.05$, $\gamma = 0.8$, the corresponding normalized stress–strain curves under uniaxial, biaxial and triaxial tension are shown in Fig. 4a. Define ε_t as the critical strain which corresponds to the strain value at the uniaxial peak-stress. The ε_t is calibrated as $\varepsilon_t = 0.0036$ through the simulated uniaxial stress–strain curve. From Fig. 4a it is seen that the three stress–strain curves agree with the tensile behaviors of the typical engineering material in that in the pre-peak stage, the stress increases with increasing strain whereas smoothly decreases with further increasing strain in the post-peak stage. In the present constitutive model, the triaxial tension strength is a little bit higher than the uniaxial tension strength.

However, when we keep other shape parameters fixed and increase r_0^* from 1.05 to 5.0, the corresponding stress–strain curves are shown in Fig. 4b. In Fig. 4b, a strong ‘ductile’ behavior is observed in the uniaxial curve in which the three-body interaction comes into play while no ‘ductile’ behavior is observed in the triaxial curve in which the three-body interaction does not play. So, we can conclude that the three-body interaction dominates the post-peak behavior. The r_0^* controls the ‘brittle’ or the ‘ductile’. If the r_0^* takes a bigger value, say 5.0, the ductile behavior can be reproduced while takes a smaller value, the brittle behavior is produced. It is very important for the parameter calibration when applying the present method.

According to Eq. (5), increasing the cutoff radius r_0^* can diminish the effect of the cutoff functions $\exp[1/(\tilde{r} - r_0^*)]$ and $\exp[\gamma/(\tilde{r} - r_0^*)]$. In the extreme case where no cutoff term is considered in the two- and three-body interaction, i.e. $\Phi_2(\tilde{r}_i) = A(B\tilde{r}_i^{-p} - \tilde{r}_i^{-q})$ and $\Phi_3(\tilde{r}_i, \tilde{r}_j, \theta_{ij}) = \lambda(\cos \theta_{ij} - \cos \theta_{j0})^2$, the ε_t at the first-peak stress is dependent on p, q . When $p = 12, q = 6$, the calibrated ε_t is approximately $\varepsilon_t \approx 0.32$. When r_0^* is smaller, both the ε_t and the uniaxial tensile strength increase with increasing r_0^* . Fig. 5a Confirms this

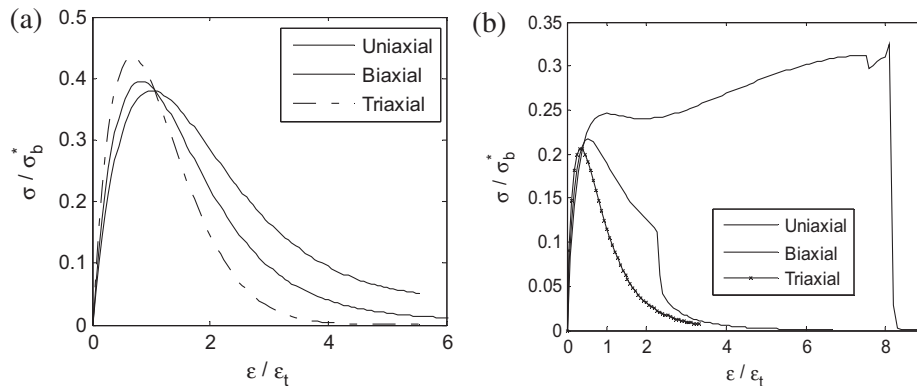


Fig. 4. Stress–strain curves under uniaxial, biaxial and triaxial tension with parameters $E = 10.0$ GPa, $\nu = 0.2$, $p = 12$, $q = 6$, $\gamma = 0.8$, (a) $r_0^* = 1.05$ (the calibrated critical uniaxial strain $\varepsilon_t \approx 0.0036$ and $\sigma_b^* = E\varepsilon_t = 10.0 \times 3.6 = 36.0$ MPa. The uniaxial tensile strength is about 13.7 MPa); (b) $r_0^* = 5.0$ (the calibrated critical uniaxial strain $\varepsilon_t \approx 0.3$ and $\sigma_b^* = E\varepsilon_t = 10.0 \times 300.0 = 3000.0$ MPa. The uniaxial tensile strength is about 900.0 MPa).

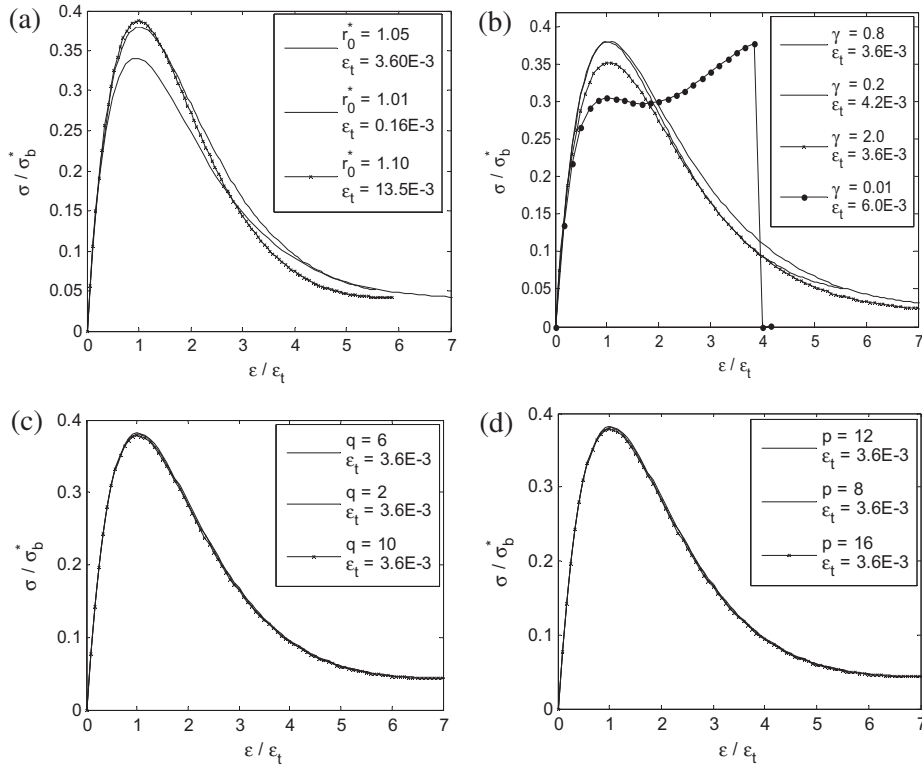


Fig. 5. Influence of micro parameters on uniaxial tensile stress–strain response (a) effect of r_0^* ($p = 12, q = 6, \gamma = 0.8$); (b) effect of γ ($p = 12, q = 6, r_0^* = 1.05$); (c) effect of q ($p = 12, r_0^* = 1.05, \gamma = 0.8$); (d) effect of p ($q = 6, r_0^* = 1.05, \gamma = 0.8$). (In all cases, $E = 10.0$ GPa, $\nu = 0.2$.)

trend. With r_0^* further increasing, both ϵ_t and the uniaxial tensile strength approach to their upper bound. It is noted that when $r_0^* = 5.0$, the critical strain is $\epsilon_t \approx 0.3$, which is close to its upper bound $\epsilon_t \approx 0.32$ and the corresponding uniaxial strength is about 900 MPa.

Figs. 5b and c display the influence of the shape parameters γ, q, p at $r_0^* = 1.05$. From Fig. 5b, an interesting phenomenon is observed namely that both the ϵ_t and the uniaxial tensile strength increase with decreasing γ when the γ is smaller than a certain value. And the uniaxial stress–strain curve becomes strongly ‘ductile’ when γ is smaller than a certain value. In contrast to the r_0^* and γ , the p, q seem to have no influence on the stress–strain response when they varies between 6 and 16 in the case of $r_0^* = 1.05$ and $\gamma = 0.8$, shown as Fig. 5c and d. Fig. 5 provides a valuable reference for the parameter calibration in using the present method.

5. Constitutive relation based on linear SW potential

5.1. Constitutive relation

The bond length and the bond angle are two quantities that characterize the energy of a discrete system governed by SW potential. The SW potential is a nonlinear function of the two quantities. In the linear elastic case, the two- and three-body potential can be written as

$$\begin{aligned}\Phi_2 &= \frac{1}{2}A(r_l - \ell_0)^2 \\ \Phi_3 &= \frac{1}{2}\lambda(\theta_{ij} - \theta_{ij0})^2\end{aligned}\quad (37)$$

Substituting Eq. (37) into Eqs. (17), (18), we have the stress tensor

$$\begin{aligned}\sigma_{ij} &= \bar{k}_n / \ell_0^2 \cdot \langle (r_l - \ell_0) \ell_0 \cdot \xi_i \xi_j \rangle_2 + \bar{k}_s \cdot \langle (\theta_{ij} - \theta_{ij0}) \cdot \Theta_{ij} \rangle_3 \\ &= \bar{k}_n \cdot \langle \xi^T \xi \xi \cdot \xi_i \xi_j \rangle_2 + \bar{k}_s \cdot \langle (\Theta : \epsilon) \cdot \Theta_{ij} \rangle_3\end{aligned}\quad (38)$$

and the tangent modulus tensor

$$K_{ijkl} = \bar{k}_n \cdot \langle \xi_i \xi_j \xi_k \xi_l \rangle_2 + \bar{k}_s \cdot \langle \Theta_{ij} \Theta_{kl} \rangle_3 \quad (39)$$

in which

$$\bar{k}_n = \frac{D_l \ell_0^2 A}{2V}, \quad \bar{k}_s = \frac{D_l D_j \lambda}{2V} \quad (40)$$

5.2. Parameter calibration

5.2.1. 3D-Case

In 3D cases, the sub-Hookean matrix Ω_R^s by integrating the term $\langle \Theta_{ij} \Theta_{kl} \rangle_3$ of Eq. (39) is

$$\Omega_R^s = \frac{32\pi^2}{45} \begin{bmatrix} 4 & -2 & -2 & 0 & 0 & 0 \\ -2 & 4 & -2 & 0 & 0 & 0 \\ -2 & -2 & 4 & 0 & 0 & 0 \\ 0 & 0 & 0 & 3 & 0 & 0 \\ 0 & 0 & 0 & 0 & 3 & 0 \\ 0 & 0 & 0 & 0 & 0 & 3 \end{bmatrix} \quad (41)$$

By the same calibration process as the Section 4.1, the parameters are calibrated as

$$\bar{k}_n = \frac{3E}{4\pi(1-2\nu)}, \quad \bar{k}_s = \frac{9E(1-4\nu)}{64\pi^2(1+\nu)(1-2\nu)} \quad (42)$$

5.2.2. 2D-Case

In 2D-cases, the sub-Hookean matrix Ω_R^s by integrating the term $\langle \Theta_{ij} \Theta_{kl} \rangle_3$ is

$$\Omega_R^m = \pi^2 \begin{bmatrix} 1 & -1 & 0 \\ -1 & 1 & 0 \\ 0 & 0 & 1 \end{bmatrix} \quad (43)$$

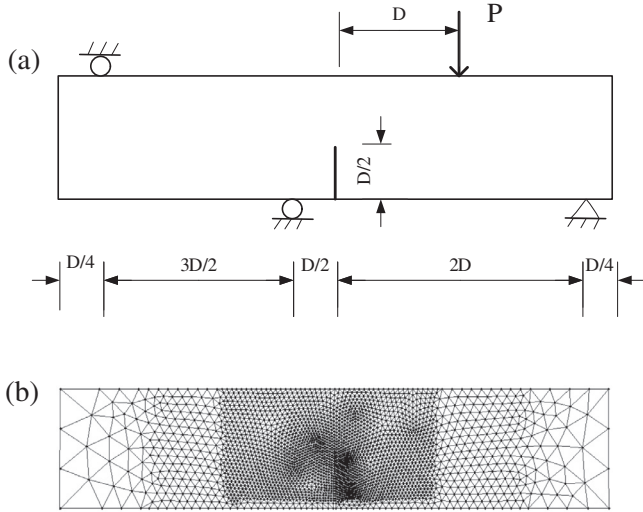


Fig. 6. Simulation objects (a) four-point-bend specimen; (b) meshing scheme. ($D = 150$ mm).

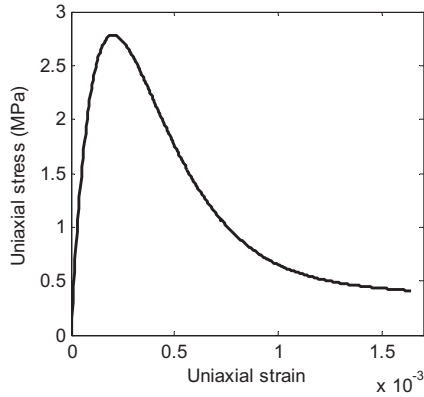


Fig. 7. The calibrated uniaxial stress–strain curve for four-point-bend test simulation.

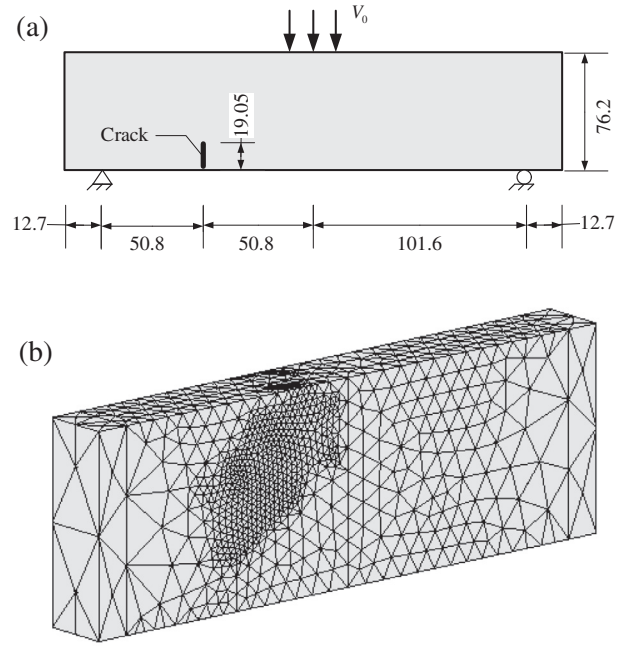


Fig. 9. Simulation object for dynamic fracture growth (a) dimensions (Unit: mm) and boundary conditions, the thickness $B = 25.4$ mm; (b) illustration of meshing scheme.

By the same way, the parameters are calibrated as

$$\bar{k}_n = \frac{E_0}{\pi(1 - \nu_0)}, \quad \bar{k}_s = \frac{E_0(1 - 3\nu_0)}{4\pi^2(1 - \nu_0^2)} \quad (44)$$

From the parameter calibration process, it is interesting to note that though the integrand of Eq. (39), say $\Theta_{ij}\Theta_{kl}$, is different from that of Eq. (21), say $\sin^2 \theta_{ij0} \cdot \Theta_{ij}\Theta_{kl}$, their Hookean matrixes combined with the that of $\langle \xi_i \xi_j \xi_k \xi_l \rangle_2$ are consistent with the Hookean matrix of the linear elasticity. Therefore, a corresponding relationship between the micro bond parameters and macro material constants exists.

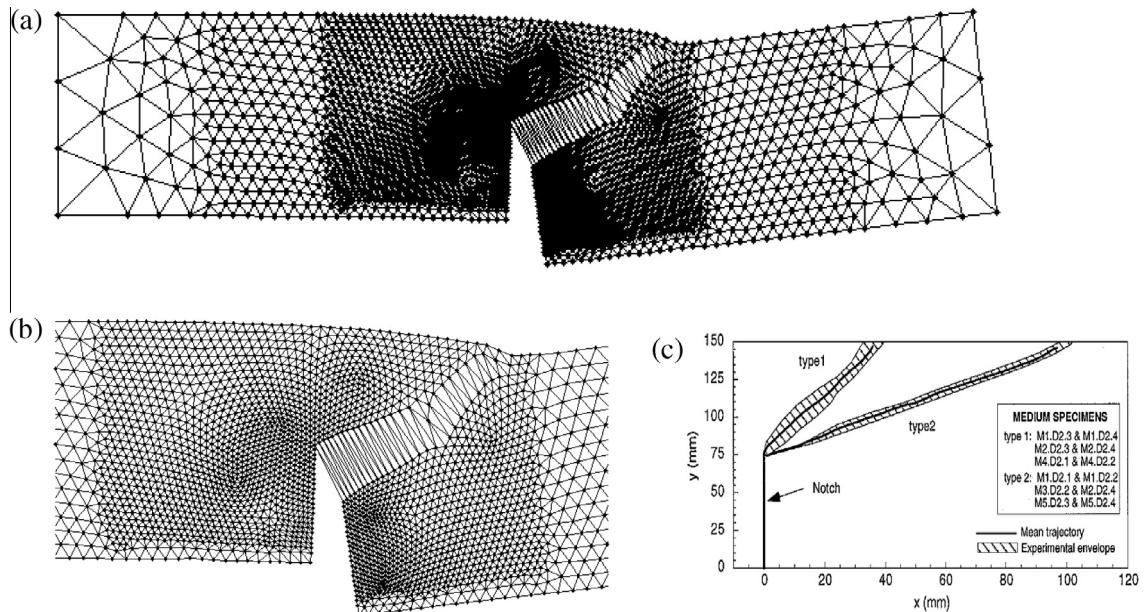


Fig. 8. Simulated fracture trajectory in the four-point-bend test (a) overview; (b) fracture zoomed in; (c) the experimental observation reported in Galvez et al. (1998) (corresponding to the Type 2).

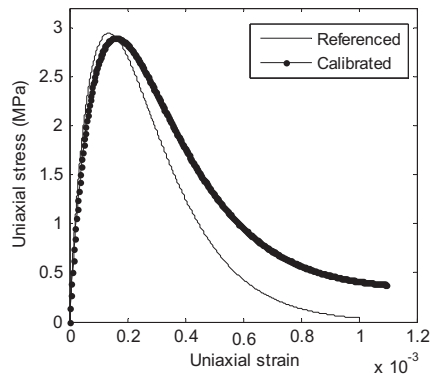


Fig. 10. The uniaxial stress–strain curves. (The reference stress–strain curve is rebuilt by the given parameters and Eq. (B.5) of Song et al. (2006)).

Based on the linear SW potential (Eq. (37)), we could develop different nonlinear angle-dependent potentials for materials. Eqs. (42) and (44) provide the corresponding micro–macro parameter relationship for the developed angle-dependent potentials.

6. Applications to fracture simulation

6.1. Fracture growth in concrete under quasi-static load

To examine whether the present method can be used to material other than the silicon, we use it to simulate a four-point-bend test of concrete (Fig. 6a) reported in Galvez et al. (1998). The tetrahedral element is adopted and the meshing scheme is shown in Fig. 6b, in which the total element number is 5161 and the total node number is 2674.

According to the parameters provided in Galvez et al. (1998): Young's modulus $E = 38.4$ GPa and the uniaxial tensile strength

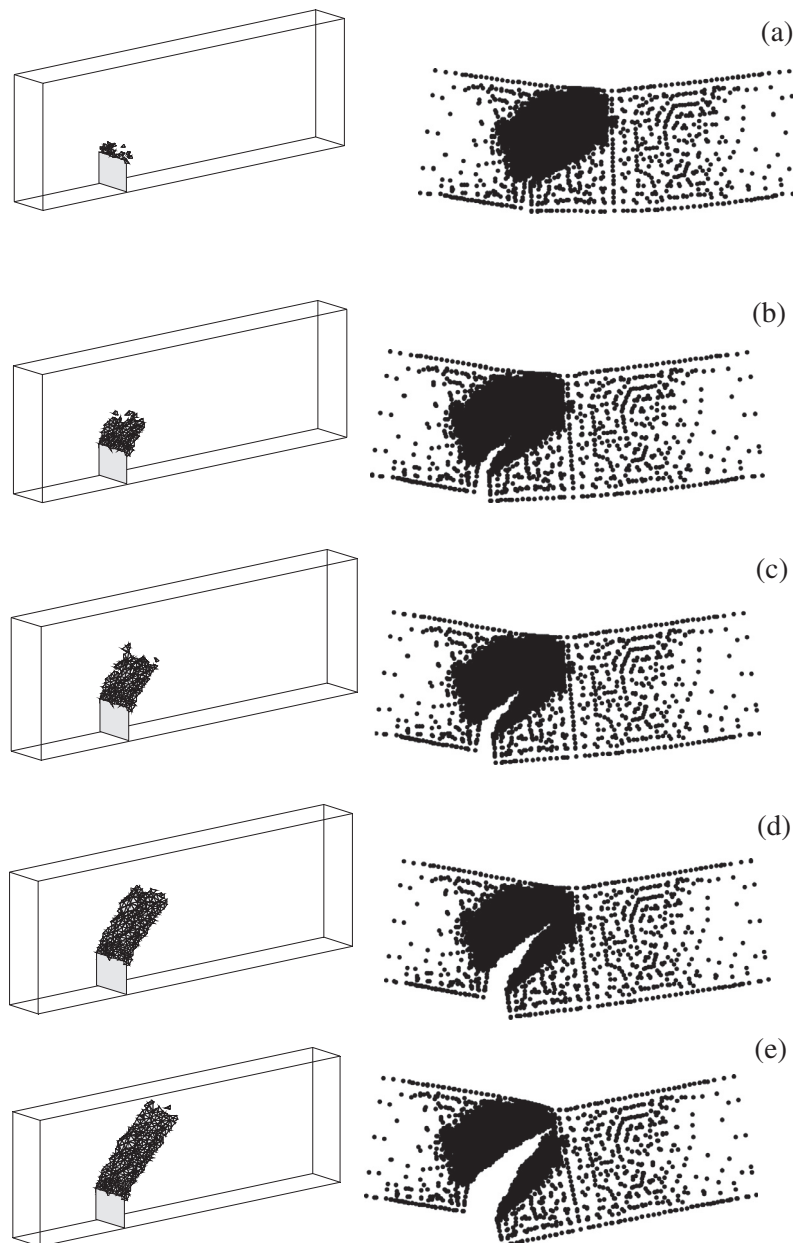


Fig. 11. Crack growth process at the (a) 286th μ s; (b) 312th μ s; (c) 325th μ s; (d) 345th μ s; (e) 385th μ s (the pictures at the left column are the extended crack faces while those at the right column are the configuration of nodes with displacement magnified 1000 times.).

$f_t = 2.8$ MPa, we calibrated the model parameter as $r_0^* = 1.012$ if taking $\nu = 0.12$, $p = 12$, $q = 6$, and $\gamma = 0.8$. The calibrated stress–strain relationship is shown in Fig. 7, according to which $\varepsilon_t = 2.0276 \times 10^{-4}$ and the corresponding uniaxial tensile strength is $f_t = 2.78$ MPa.

Take the displacement-control loading scheme with each step -0.0002 mm. The simulated fracture trajectory is shown in Fig. 8a and b. From Fig. 8a and b, it is seen that the fracture grows towards the right side and curves up-wards, which agrees with experimental observation (Fig. 8c Type 2) reported in Galvez et al. (1998). This suggests that the present method can capture the characters of the fracture growth in quasi-brittle material.

6.2. Dynamic fracture growth in concrete under impact load

To further examine the application of the present method to other materials, we use it to simulate a 3D beam of concrete (Fig. 9a) with an offset crack under the impact load, reported in John (1988), Belytschko and Tabbara (1996), Song et al. (2006). The beam is subjected to the velocity (Belytschko and Tabbara, 1996)

$$v_0(t) = \begin{cases} v_1 t / t_1 & \text{for } t \leq t_1 \\ v_1 & \text{for } t > t_1 \end{cases} \quad (45)$$

at the upper edge shown as Fig. 9a, where $t_1 = 1.96 \times 10^{-4}$ s.

The tetrahedral element is used. The meshing scheme is illustrated in Fig. 9b. The node number is 5899 and the element number is 30,053. To calibrate the input parameters of the present method, we firstly rebuilt the uniaxial tensile stress–strain relationship according to the provided parameters and Eq. (B.5) of Song et al. (2006). And then according to this stress–strain curve, we calibrated the input parameters as: $E = 50.0$ GPa, $r^* = 1.0103$, $\nu = 0.2$, $p = 12$, $q = 6$, $\gamma = 0.8$. The rebuilt and the calibrated uniaxial stress–strain relationships are shown in Fig. 10, according to

which the calibrated $\varepsilon_t = 1.6166 \times 10^{-4}$ and the uniaxial tensile strength $\sigma_b = 2.895$ MPa.

According to Fig. 10, it can be found that when the deformation is approximately smaller than $0.5\varepsilon_t$, the stress–strain relationship is almost linear. To reduce the computation burden, we only adopt the present constitutive relation when the first principle strain of element is bigger than $0.5\varepsilon_t$. For the elements whose first principle strain is smaller than $0.5\varepsilon_t$, we use the linear elastic constitutive relation. In this simulation, we use the explicit integration scheme and take time interval $\Delta t = 0.05 \mu\text{s}$. Because no separate fracture criterion is adopted in the present paper, the fracture surface is approximately presented by the array of the overstretched elements. The overstretched element, here, refers to such element whose first principle strain exceeds $5\varepsilon_t$. Fig. 11 shows the fracture growth process. From Fig. 11 it is seen that the crack begins to grow approximately at the 286th μs and the whole growth process lasts approximate 100 μs . The fracture grows towards the impact point. The simulated starting time of fracture growth is earlier than that simulated in Song et al. (2006). This is because no any regularization method is adopted in the present paper so that the fracture energy could not be preserved during the element softening. The present constitutive relation is a strain-softening one. The common feature of the strain-softening constitutive models is that they suffer from the element size sensitivity problem. To remedy the element size sensitivity problem, many regularization methods have been proposed, e.g. Zhang and Gao (2012). The main purpose of the present example is to check whether the present method can simulate the fracture propagation, so we do not introduce the regularization method in the present paper.

It is interesting to note that the crack frontier does not move smoothly forwards at the first half propagation process, but jumpily, shown in Fig. 11a and b. This might result from the fact that amount of stain energy stored in the specimen tends to release quickly when the crack starts to grow. At this stage, the crack

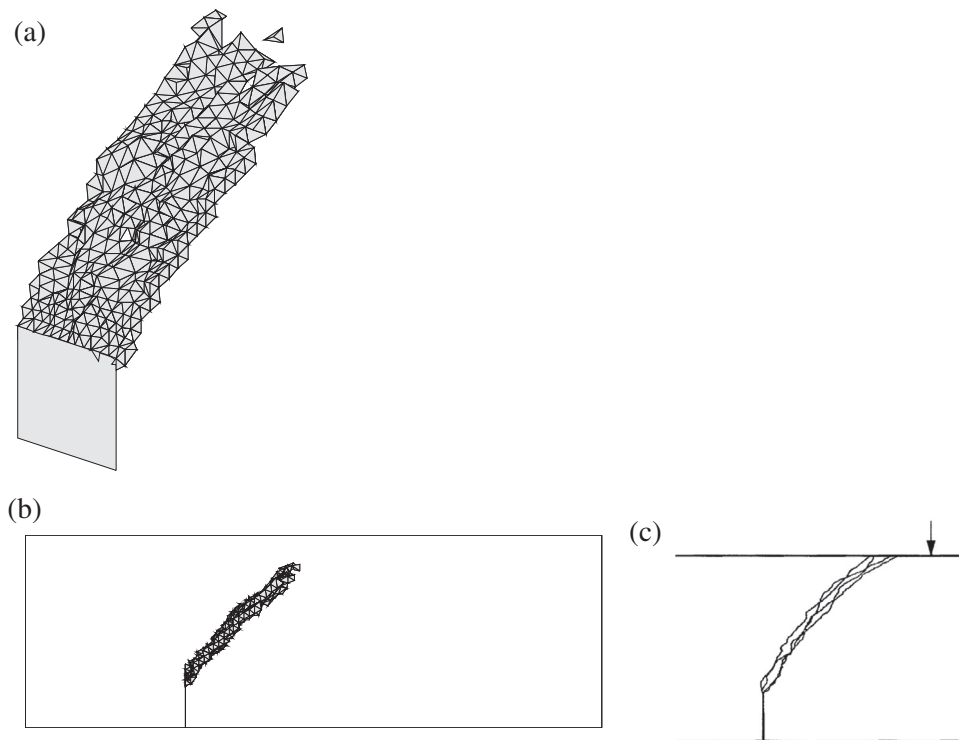


Fig. 12. The final crack face (a) the crack face zoomed in at the 385th μs ; (b) the crack face viewed from the lateral side of specimen at the 385th μs ; (c) the sketch of crack trajectories observed in the experiment (John, 1988; Belytschko and Tabbara, 1996).

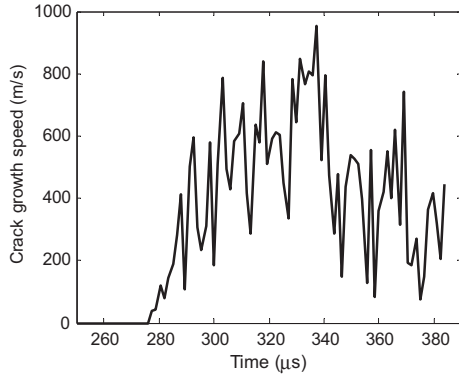


Fig. 13. Crack growth speed (the average speed over 1.5 μs).

grows at a higher speed, indicated as Fig. 13. In the second half propagation process, the crack frontier moves forwards more smoothly, shown in Fig. 11c–e. And at this stage, the crack grow speed becomes lower, indicated as Fig. 13.

The final extended crack surface is shown as Fig. 12a, from which it is seen that the crack surface is not smooth, but a rough one. The rough crack surface created in the fracture experiment of quasi-brittle materials is very popular. The crack trajectory viewed from the lateral side of specimen (Fig. 12b) is similar to that (Fig. 12c) observed in the experiment (John, 1988; Belytschko and Tabbara, 1996).

The 3D fracture simulation is quite different from the 2D case. It is difficult to directly obtain the line speed of crack growth. To obtain the line speed of crack growth, we firstly get the average crack face creation speed over the time interval $30\Delta t = 1.5 \mu s$. Then dividing the crack face creation speed with the thickness (25.4 mm) of specimen, we obtain the line speed of the crack growth, shown in Fig. 13. From Fig. 13 it is seen that the crack grow faster at the first half propagation process than the second half process generally. During the whole propagation process, the crack speed is not constant, but fluctuated. The fluctuation of dynamic crack growth speed can be found in many literatures, e.g. Song et al. (2006).

According to this dynamic fracture example, it is suggested that the present method can capture most of the characters of the dynamic crack propagation.

7. Conclusion remarks

The original SW potential is modified in that the value of the bond angle in the reference configuration, not the 'ideal' tetrahedral angle, is taken as the reference value of this bond angle in the current configuration. Based on this modified SW potential, a constitutive model is developed. By this method, the micro fracture mechanism invoked in the SW potential is incorporated into the constitutive relation. It is found that the Hookean matrix derived from the modified SW potential matches that of the linear elastic material. This suggests that there exists a corresponding relationship between the physical parameters of SW potential and the material constants. And the corresponding relationship has been derived.

The SW potential incorporated constitutive model can reproduce the brittle and ductile behaviors, depending on its input parameters. The application example of the present method to simulating fracture growth in concrete suggests that the present method can capture most of the characters of the fracture propagation in the quasi-brittle materials both in dynamic and static load.

The constitutive model based on the modified SW potential can be used to materials other than the silicon materials. It provides a new constitutive model for fracture analysis of nonlinear elasticity. Moreover, the derived micro–macro parameter relationship provides a parameter calibration method for SW potential.

Acknowledgments

The present work is supported by the National Natural Science Foundation of China (Grant No. 11172172) and the National Basic Research Program of China (Grant No. 2011CB013505), which are gratefully acknowledged.

Appendix A

The first derivatives of Φ_2, Φ_3 with respect to bond length r and bond angle θ_{ij} are

$$\begin{aligned}\frac{\partial \Phi_2}{\partial r_i} &= A \cdot \exp(h_i^{-1}) \left[(-Bp\tilde{r}_i^{-p-1} + q\tilde{r}_i^{-q-1}) - h_i^{-2} (B\tilde{r}_i^{-p} - \tilde{r}_i^{-q}) \right] \cdot \frac{1}{\ell_0} \\ \frac{\partial \Phi_2}{\partial r_j} &= \lambda (\cos \theta_{ij} - \cos \theta_{j0})^2 \exp(\gamma h_i^{-1}) \exp(\gamma h_j^{-1}) \cdot (-\gamma h_i^{-2}) \cdot \frac{1}{\ell_0} \\ \frac{\partial \Phi_2}{\partial \theta_{ij}} &= \lambda (\cos \theta_{ij} - \cos \theta_{j0})^2 \exp(\gamma h_i^{-1}) \exp(\gamma h_j^{-1}) \cdot (-\gamma h_j^{-2}) \cdot \frac{1}{\ell_0} \\ \frac{\partial \Phi_3}{\partial \theta_{ij}} &= \lambda \exp(\gamma h_i^{-1}) \exp(\gamma h_j^{-1}) \cdot 2(\cos \theta_{ij} - \cos \theta_{j0})(-\sin \theta_{ij})\end{aligned}\quad (A.1)$$

and the second derivatives of Φ_2, Φ_3 with respect to r and θ_{ij} are

$$\begin{aligned}\frac{\partial^2 \Phi_2}{\partial r_i^2} &= A \cdot \exp(h_i^{-1}) \left[Bp(p+1)\tilde{r}_i^{-p-2} - q(q+1)\tilde{r}_i^{-q-2} \right. \\ &\quad \left. + 2h_i^{-2} (Bp\tilde{r}_i^{-p-1} - q\tilde{r}_i^{-q-1}) + (h_i^{-4} + 2h_i^{-3})(B\tilde{r}_i^{-p} - \tilde{r}_i^{-q}) \right] \cdot \frac{1}{\ell_0^2} \\ \frac{\partial^2 \Phi_2}{\partial r_i^2} &= \lambda (\cos \theta_{ij} - \cos \theta_{j0})^2 \exp(\gamma h_j^{-1}) \exp(\gamma h_i^{-1}) (\gamma^2 h_i^{-4} + 2\gamma h_i^{-3}) \cdot \frac{1}{\ell_0^2} \\ \frac{\partial^2 \Phi_2}{\partial r_j^2} &= \lambda (\cos \theta_{ij} - \cos \theta_{j0})^2 \exp(\gamma h_i^{-1}) \exp(\gamma h_j^{-1}) (\gamma^2 h_j^{-4} + 2\gamma h_j^{-3}) \cdot \frac{1}{\ell_0^2} \\ \frac{\partial^2 \Phi_2}{\partial \theta_{ij}^2} &= \lambda \exp(\gamma h_i^{-1}) \exp(\gamma h_j^{-1}) \cdot 2(1 - 2\cos^2 \theta_{ij} + \cos \theta_{j0} \cos \theta_{ij})\end{aligned}\quad (A.2)$$

Appendix B

If the bonds are uniformly distributed and the bond number Ω is large enough, the bond distribution density D_l is a constant, which can be determined as

$$\begin{aligned}\int_0^{2\pi} \int_0^\pi D_l \sin \alpha \cdot d\alpha d\varphi &= \Omega \Rightarrow D_l = \frac{\Omega}{4\pi} \quad \text{in 3D-case} \\ \int_0^{2\pi} D_l &= \Omega \Rightarrow D_l = \frac{\Omega}{2\pi} \quad \text{in 2D-case}\end{aligned}\quad (B.1)$$

By Eq. (B.1), the bond number in the small volume $\sin \alpha \cdot \Delta \alpha \Delta \varphi$ in the spherical coordinates is $D_l \sin \alpha \cdot \Delta \alpha \Delta \varphi$, in which the intervals $\Delta \alpha, \Delta \varphi$ are $\Delta \alpha = \pi/M, \Delta \varphi = 2\pi/Q$ with M, Q being the interval number in the coordinates α, φ , respectively, shown in Fig. B1. So the first term of Eq. (8) can be written as

$$\begin{aligned}\frac{1}{V} \cdot \frac{1}{2} \cdot \sum_{l=1}^{N(N-1)} \Phi_2(r_l) &= \frac{1}{2V} \sum_{q=1}^Q \sum_{m=1}^M \Phi_2(\xi(\alpha_m, \varphi_q)) D_l \sin \alpha_m \cdot \Delta \alpha \Delta \varphi \\ &= \frac{1}{2V} \int_0^{2\pi} \int_0^\pi \Phi_2(\xi(\alpha_m, \varphi_q)) D_l \sin \alpha \cdot d\alpha d\varphi \quad \text{if} \\ M &\rightarrow \infty, Q \rightarrow \infty\end{aligned}\quad (B.2)$$

in which $D_l = N(N-1)/(4\pi)$.

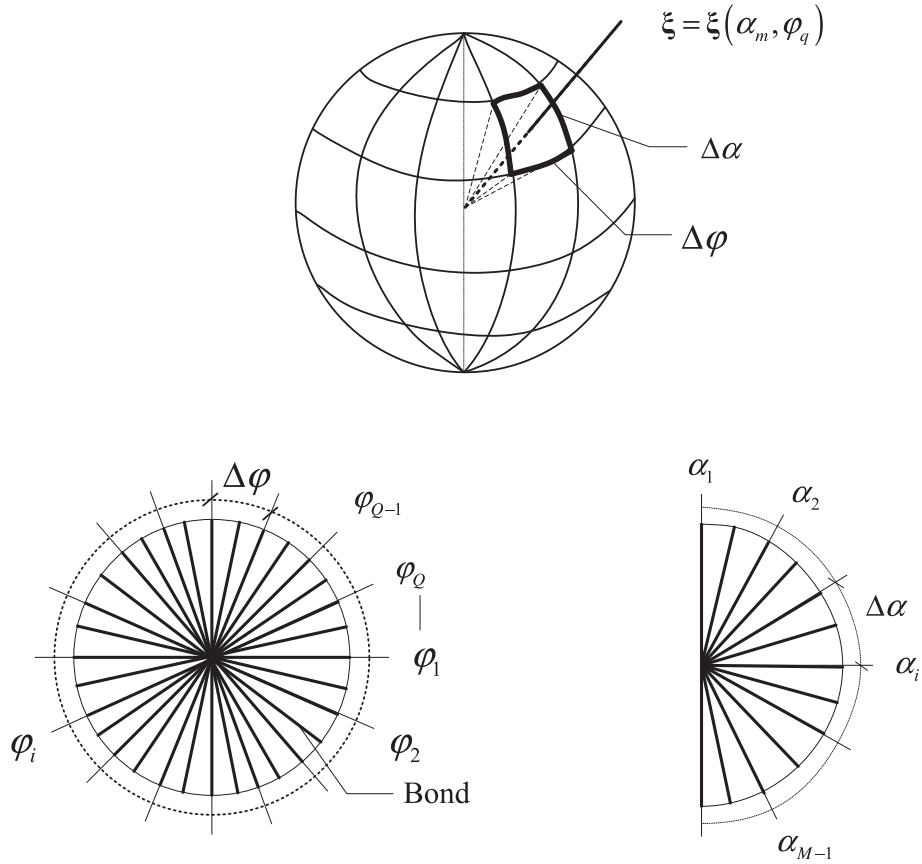


Fig. B1. Bond distribution discretization in which the bond sphere is equally discretized into M intervals with the dimension α and Q intervals with the dimension φ .

The second term of Eq. (8) can be written as

$$\begin{aligned}
 & \frac{1}{V} \cdot \frac{1}{2} \cdot \sum_{l=1}^{N(N-1)} \sum_{j \neq l}^{N-2} \Phi_3(r_l, r_j, \theta_{lj}) \\
 &= \frac{1}{2V} \sum_{l=1}^{N(N-1)} \sum_{j \neq l}^{N-2} \Phi_3(\xi_l, \eta_j) \\
 &= \frac{1}{2V} \sum_{l=1}^{N(N-1)} \left[\sum_{q=1}^Q \sum_{m=1}^M \Phi_3(\xi_l(\alpha, \varphi), \eta(\bar{\alpha}_m, \bar{\varphi}_q)) \cdot D_j \cdot \sin \bar{\alpha}_m \cdot \Delta \bar{\alpha} \Delta \bar{\varphi} \right] \\
 &= \frac{1}{2V} \sum_{l=1}^{N(N-1)} \left[\int_0^{2\pi} \int_0^\pi \Phi_3(\xi_l(\alpha, \varphi), \eta(\bar{\alpha}, \bar{\varphi})) D_j \sin \bar{\alpha} \cdot d\bar{\alpha} d\bar{\varphi} \right] \\
 &= \frac{1}{2V} \sum_{q=1}^Q \sum_{m=1}^M \left[\int_0^{2\pi} \int_0^\pi \Phi_3(\xi(\alpha_m, \varphi_q), \eta(\bar{\alpha}, \bar{\varphi})) D_j \sin \bar{\alpha} \cdot d\bar{\alpha} d\bar{\varphi} \right] \cdot D_l \sin \alpha_m \cdot \Delta \alpha \Delta \varphi \\
 &= \frac{1}{2V} \int_0^{2\pi} \int_0^\pi \left[\int_0^{2\pi} \int_0^\pi \Phi_3(\xi(\alpha, \varphi), \eta(\bar{\alpha}, \bar{\varphi})) D_j \sin \bar{\alpha} \cdot d\bar{\alpha} d\bar{\varphi} \right] D_l \sin \alpha \cdot d\alpha d\varphi \\
 &= \frac{1}{2V} \int_0^{2\pi} \int_0^\pi \int_0^{2\pi} \int_0^\pi \Phi_3(\xi(\alpha, \varphi), \eta(\bar{\alpha}, \bar{\varphi})) \cdot D_l D_j \sin \bar{\alpha} \cdot \sin \alpha \cdot d\bar{\alpha} d\bar{\varphi} d\alpha d\varphi
 \end{aligned} \tag{B.3}$$

in which $D_j = (N-2)/(4\pi)$.

By the same way, in 2D cases, the first term of Eq. (8) can be written as

$$\frac{1}{V} \cdot \frac{1}{2} \cdot \sum_{l=1}^{N(N-1)} \Phi_2(r_l) = \frac{1}{2V} \sum_{m=1}^M \Phi_2(\xi(\alpha_m)) D_l \cdot \Delta \alpha = \frac{1}{2V} \int_0^{2\pi} \Phi_2(\xi(\alpha)) D_l \cdot d\alpha \quad \text{if } M \rightarrow \infty \tag{B.4}$$

and the second term of Eq. (8) can be written as

$$\begin{aligned}
 \frac{1}{V} \cdot \frac{1}{2} \cdot \sum_{l=1}^{N(N-1)} \sum_{j \neq l}^{N-2} \Phi_3(r_l, r_j, \theta_{lj}) &= \frac{1}{2V} \sum_{l=1}^{N(N-1)} \sum_{j \neq l}^{N-2} \Phi_3(\xi_l, \eta_j) \\
 &= \frac{1}{2V} \sum_{l=1}^{N(N-1)} \left[\sum_{m=1}^M \Phi_3(\xi_l(\alpha), \eta(\bar{\alpha}_m)) \cdot D_j \cdot \Delta \bar{\alpha} \right] \\
 &= \frac{1}{2V} \sum_{l=1}^{N(N-1)} \left[\int_0^{2\pi} \Phi_3(\xi_l(\alpha), \eta(\bar{\alpha})) D_j d\bar{\alpha} \right] \\
 &= \frac{1}{2V} \sum_{m=1}^M \left[\int_0^{2\pi} \Phi_3(\xi(\alpha_m), \eta(\bar{\alpha})) D_j d\bar{\alpha} \right] D_l \cdot \Delta \alpha \\
 &= \frac{1}{2V} \int_0^{2\pi} \int_0^{2\pi} \Phi_3(\xi(\alpha), \eta(\bar{\alpha})) D_j D_l \cdot d\bar{\alpha} d\alpha
 \end{aligned} \tag{B.5}$$

in which $D_l = N(N-1)/(2\pi)$, $D_j = (N-2)/(2\pi)$.

By Eqs. (B.2)–(B.5), Eq. (9) can be obtained.

Appendix C

Let

$$T = T(\mathbf{E}) = \frac{2\xi^T \mathbf{E} \boldsymbol{\eta} + \xi^T \boldsymbol{\eta}}{\sqrt{2\xi^T \mathbf{E} \xi + \xi^T \xi} \cdot \sqrt{2\boldsymbol{\eta}^T \mathbf{E} \boldsymbol{\eta} + \boldsymbol{\eta}^T \boldsymbol{\eta}}} = \frac{Q_{12}}{\sqrt{Q_{11}} \cdot \sqrt{Q_{22}}} \tag{C.1}$$

in which the scalars Q_{12} , Q_{11} and Q_{22} are respectively

$$\begin{aligned}
 Q_{12} &= 2\xi_p E_{pq} \eta_q + \xi_m \eta_m \\
 Q_{11} &= 2\xi_p E_{pq} \xi_q + \xi_m \xi_m \\
 Q_{22} &= 2\eta_p E_{pq} \eta_q + \eta_m \eta_m
 \end{aligned} \tag{C.2}$$

According to Eq. (7), the angle θ_{ij} can be calculated as

$$\theta_{ij}(\mathbf{E}) = \arccos(T) \quad (\text{C.3})$$

The first derivative of $\theta_{ij}(\mathbf{E})$ with respect to \mathbf{E} is

$$\begin{aligned} \frac{\partial \theta_{ij}}{\partial E_{ij}} &= -\frac{1}{\sqrt{1-T^2}} \cdot \frac{\partial T}{\partial E_{ij}} \\ &= -\frac{1}{\sqrt{1-T^2}} \cdot \frac{1}{\sqrt{Q_{11}Q_{22}}} \left(2\xi_i \eta_j - \frac{Q_{12}}{Q_{11}} \cdot \xi_i \xi_j - \frac{Q_{12}}{Q_{22}} \cdot \eta_i \eta_j \right) \end{aligned} \quad (\text{C.4})$$

Under the undeformed state, according to Eqs. (C.1) and (C.2), the following relationship holds

$$T = Q_{12} = \xi^T \boldsymbol{\eta}, \quad Q_{11} = 1, \quad Q_{22} = 1 \quad (\text{C.5})$$

By Eqs. (C.4) and (C.5), Eq. (16) can be obtained.

Appendix D. Supplementary data

Supplementary data associated with this article can be found, in the online version, at <http://dx.doi.org/10.1016/j.ijssolstr.2014.01.003>.

References

- Belytschko, T., Tabbara, M., 1996. Dynamic fracture using element-free Galerkin methods. *Int. J. Numer. Methods Eng.* 39, 923–938.
- Brenner, D.W., 1990. Empirical potential for hydrocarbons for use in simulation the chemical vapor deposition of diamond films. *Phys. Rev. B* 42, 9458–9471.
- Chang, C.S., Hicher, P.Y., 2005. An elasto-plastic model for granular materials with microstructural consideration. *Int. J. Solids Struct.* 42, 4258–4277.
- Daw, M.S., Baskes, M.I., 1983. Semiempirical, quantum mechanical calculation of hydrogen embrittlement in metals. *Phys. Rev. Lett.* 50, 1285–1288.
- Galvez, J.C., Elices, M., Guinea, G.V., Planas, J., 1998. Mixed mode fracture of concrete under proportional and nonproportional loading. *Int. J. Fract.* 94, 267–284.
- Gao, H.J., Klein, P., 1998. Numerical simulation of crack growth in an isotropic solid with randomized internal cohesive bond. *J. Mech. Phys. Solids* 46, 187–218.

- He, M.H., Li, S.F., 2012. An embedded atom hyperelastic constitutive model and multiscale cohesive finite element method. *Comput. Mech.* 49, 337–355.
- John, R., 1988. Mixed Mode Fracture of Concrete Subjected to Impact Loading (Ph.D. Dissertation). Northwestern University.
- Li, S.F., Zeng, X.W., Ren, B., Qian, J., Zhang, J.S., Jha, A.K., 2012. An atomistic-based interphase zone model for crystalline solids. *Comput. Methods Appl. Mech. Eng.* 229–232, 87–109.
- Liu, X.H., Gu, J.F., Shen, Y., Li, J., Chen, C.F., 2010. Lattice dynamical finite-element method. *Acta Mater.* 58, 510–523.
- Milstein, F., 1980. Review: theoretical elastic behavior at large strains. *J. Mater. Sci.* 15, 1071–1084.
- Misra, A., Yang, Y., 2010. Micromechanical model for cohesive materials based upon pseudo-granular structure. *Int. J. Solids Struct.* 47, 2970–2981.
- Pizzagalli, L., Godet, J., Guenole, J., Brochard, S., Holmstrom, E., Nordlund, K., Albaret, T., 2013. A new parametrization of the Stillinger–Weber potential for an improved description of defects and plasticity of silicon. *J. Phys. Condens. Matter* 25, 055801.
- Song, J.H., Areias, P.M.A., Belytschko, T., 2006. A method for dynamic crack and shear band propagation with phantom nodes. *Int. J. Numer. Methods Eng.* 67, 868–893.
- Stillinger, F.H., Weber, T.A., 1985. Computer simulation of local order in condensed phases of silicon. *Phys. Rev. B* 31, 5262–5271.
- Tadmor, E.B., Ortiz, M., Phillips, R., 1996. Quasicontinuum analysis of defects in solids. *Philos. Mag. A* 73, 1529–1563.
- Tersoff, J., 1988. New empirical approach for the structure and energy of covalent systems. *Phys. Rev. B* 37, 6991–7000.
- Xu, X.P., Needleman, A., 1994. Numerical simulations of fast crack growth in brittle solids. *J. Mech. Phys. Solids* 42, 1397–1434.
- Zeng, X.W., Li, S.F., 2010. A multiscale cohesive zone model and simulations of fractures. *Comput. Methods Appl. Mech. Eng.* 199, 547–556.
- Zhang, Z.N., Gao, H.J., 2012. Simulating fracture propagation in rock and concrete by an augmented virtual internal bond method. *Int. J. Numer. Anal. Methods Geomech.* 36, 459–482.
- Zhang, Z.N., Ge, X.R., 2005. A new quasi-continuum constitutive model for crack growth in an isotropic solid. *Eur. J. Mech. – A/Solids* 24, 243–252.
- Zhang, Z.N., Ge, X.R., 2006. Micromechanical modelling of elastic continuum with virtual multi-dimensional internal bonds. *Int. J. Numer. Methods Eng.* 65, 135–146.
- Zhang, P., Huang, Y., Geubelle, P.H., Klein, P.A., Hwang, K.C., 2002. The elastic modulus of single-wall carbon nanotubes: a continuum analysis incorporating interatomic potentials. *Int. J. Solids Struct.* 39, 3893–3906.
- Zhao, S.F., Zhao, G.F., 2012. Implementation of a high order lattice spring model for elasticity. *Int. J. Solids Struct.* 49, 2568–2581.